Gravity affects magma-induced crustal deformation: comparing laccoliths on the Moon, Mars, and Earth

S. Poppe[1], A. Cornillon[1,2], A. Morand[1,3], and C. E. Harnett[4]

[1] Centrum Badań Kosmicznych Polskiej Akademi Nauk, Bartycka 18A, 00-716 Warsaw, Poland.
[2] Département de Géosciences, École Normale Supérieure, CNRS UMR 8538, PSL Université, Paris, France.
[3] School of Earth Sciences, Bristol University, United Kingdom.
[4] UCD School of Earth Sciences, University College Dublin, Belfield, Dublin 4, Ireland.
*contact: sampoppe@cbk.waw.pl, sam35poppe@gmail.com

Please refer to this work as:
Poppe, S., Cornillon, A., Morand, A., Harnett, C. (2024). Gravity affects magma-induced crustal deformation: comparing the Moon, Mars, and Earth. *Preprint, EarthArxiv*.

Gravity affects magma-induced crustal deformation: comparing the Moon, Mars, and Earth

S. Poppe[1], A. Cornillon[1,2], A. Morand[1,3], and C. E. Harnett[4]

[1]Centrum Badań Kosmicznych Polskiej Akademi Nauk, Bartycka 18A, 00-716 Warsaw, Poland. [2]Département de Géosciences, École Normale Supérieure, CNRS UMR 8538, PSL Université, Paris, France. [3]School of Earth Sciences, Bristol University, United Kingdom. [4]UCD School of Earth Sciences, University College Dublin, Belfield, Dublin 4, Ireland.

Corresponding author: Sam Poppe (sampoppe@cbk.waw.pl and sam35poppe@gmail.com)

Key Points:

- Inflation of a magmatic laccolith at gravity of the Moon, Mars, and Earth was implemented in the two-dimensional Discrete Element Method.
- Simulations show that the magma-induced fracturing accumulates in narrower zones in weaker rock at lower gravity.
- Simulations show that laccolith inflation induces more surface displacement over a wider area at lower gravity, and opens longer and wider cracks in the crust.

Abstract

Dome-shaped, uplifted surface areas and associated fractures on Mars and the Moon are inferred to result from the shallow emplacement of magma intrusions. This inference originates from analogue observations at partially eroded or active volcanic systems on Earth. Computational models help estimating the geometry and emplacement depth of those inferred magma bodies. Models often do not consider that the gravitational acceleration is different on planetary bodies with different masses, however, and have not simulated large concentrations of magma-induced strain and dynamic fracturing of the host rocks. We used the two-dimensional Discrete Element Method (2D DEM) to simulate the inflation of a laccolith-shaped magma intrusion in particle-based assemblages of different mechanical strength, under gravitational acceleration of the Moon, Mars, and Earth. The 2D DEM model simulates the magma-induced displacements, principal stresses, and dynamic fracturing, and allows deriving shear strains in the crust. For weak rocks, the vertical surface displacement is nearly twice as high on the Moon, compared to Earth. For stronger rocks, the amount of magma-induced cracks on the Moon is half of the amount of cracks induced on Earth. Our 2D DEM simulations show, for the first time, that gravity specific to a rocky planetary body affects the pattern and amount of fracturing and surface displacement above inflating laccoliths. This calls for a careful reevaluation, and future modelling, of differences seen in the morphology of intrusive domes found on Earth, Mars and the Moon.

Plain Language Summary

Domed surface areas have been observed on the Moon and on Mars, but how they formed remains cryptic. By analogy with similar features in volcanic areas on Earth, at least some of these features were likely caused by stalling and inflation in the shallowest few kilometers of crust of laccoliths, which are magma intrusions with a convex roof and horizontal base. Gravitational acceleration is lower on the Moon than on Mars, and is lower on Mars than on Earth. With those differences in specific gravities, can we expect that similar amounts and patterns of displacement and fracturing at the lunar and martian surface were caused by laccoliths of similar dimensions? To address this question, we used the Discrete Element Method to simulate the displacement and, for the first time, progressive fracturing of host rocks around an inflating laccolith intrusion at specific gravities of the Moon, Mars, and Earth. Our results show that laccolith intrusions of similar volume cause more surface displacement on a planetary body with weaker gravity, compared to one with stronger gravity. The amount of magma-induced fracturing, however, is more affected by the host rock´s strength than by gravity. We conclude that magma-induced deformation patterns depend on a planetary body´s specific gravity and the strength of its crust. Both features need to be accounted for when inferring magma intrusion properties from surface observations on other planets and moons.

1 Introduction

Dome-shaped surface features in volcanic terrains have been related by geological observations to the emplacement of thick magma intrusions in the shallowest several kilometers of the Earth´s crust (Bunger & Cruden, 2011; Gilbert, 1877; Morgan, 2018; Pollard & Johnson, 1973). Such thick intrusions include sills (tabular, horizontal intrusions between preexisting layers of rock) and laccoliths (intrusions with a horizontal base and a convex-upward roof). The crustal stresses associated with the inflation of those intrusions induce bending of the overburden rocks that translates in a dome-shaped uplift patterns at the surface, but also host rock compaction, fracturing and faulting (Mattsson et al., 2018; Wilson et al., 2016). The scarcity of recent and well-monitored laccolith intrusion events makes understanding their intrusion dynamics challenging. The 2011-2012 emplacement and explosive eruption of a viscous rhyolite laccolith at Puyehue Cordón Caulle, in Chile, is the only recent monitored event where dome-shaped surface uplift and tensile surface fracturing were observed through satellite imagery and sparse seismic monitoring (Castro et al., 2016). To understand laccolith- and sill-induced structural deformation thus relies on geological and geophysical observations at now-solidified and exposed volcanic and igneous plumbing systems, and modelling (Bunger & Cruden, 2011; Galland et al., 2018; Magee et al., 2018; Morgan, 2018).

Areas with a dome-shaped positive topography have been observed at the surface of the Moon since the Apollo missions in the early 1970´s. Most of those domes have rough surfaces and summit pits that suggest they are the result of the extrusion of viscous lava (Ivanov et al., 2016; Lena et al., 2013; Wilhelms, 1987). Some, however, have a gentle slope, open fractures and no eruptive vents; these are likely induced by magma emplacement in the shallowest few kilometers of the lunar crust without eruption (Head & Wilson, 2017; Lena et al., 2013; Wöhler & Lena, 2009). One of the most known intrusive domes are the Valentine domes in Mare Serenitatis (Fig. 1a). Lunar intrusive domes range in diameter from less than one kilometer to more than 30 kilometers (Lena et al., 2013). Their relative scarcity is explained by the negative buoyancy of dense mafic magma in the shallowest kilometres of the less dense lunar crust, which is dominantly composed of anorthosite rocks and highly porous due to a long impact history (Wieczorek et al., 2013; Wöhler & Lena, 2009). Lunar intrusive domes also often lie in areas between proximal mare-filled impact basins where crustal extensional stresses might favor magmatic buoyancy and ascent into shallower crustal levels (McGovern et al., 2014; Thomas et al., 2015).

On Mars, high-resolution orbital imagery has allowed the detection of dome-shaped terrain in regions with distributed volcanism away from the largest Martian volcanoes, but no global-scale overview exists to date (Farrand et al., 2011; Platz et al., 2015; Rampey et al., 2007). Most of the magmatism on both Mars and the Moon is considered dominantly mafic with low viscosity (Head & Wilson, 2017; Platz et al., 2015; Vaucher et al., 2009). Some of the intrusive domes on Mars, however, lie adjacent to intrusions exposed by erosion (Fig. 1b), eruptive cones, apparent pyroclastic deposits and thick flows of felsic, viscous lava (Brož et al., 2015; Farrand et al., 2021). This association makes it likely that thick sills or laccoliths may have intruded and inflated in the shallowest few kilometers of the Martian crust. Models have confirmed the possibility of cryptodome and laccolith formation on Arcadia Planitiae, albeit in interaction with now-molten ice sheets (Farrand et al., 2011; Michaut et al., 2013).

Other sites of inferred magma-induced surface doming and fracturing on Mars and the Moon are found at ´floor-fractured craters´ (FFCs) (Fig. 1d, 1e) (Jozwiak et al., 2012; Michaut, 2011; Schultz, 1976). Floor-fractured crater morphology has been explained in the past by post-impact viscous relaxation of the crust (Bamberg et al., 2014; Hall & Solomon, 1981; Montigny et al., 2022). Models have shown, however, that impact cratering provides a lithospheric stress deficit and driving overpressure for magma to ascend below the crater floor (Michaut & Pinel, 2018). There, the magma may then have inflated a sill or laccolith and further fractured and uplifted the overburden rocks (Michaut et al., 2020; Michaut & Pinel, 2018; Wöhler & Lena, 2009). Observations of gravity anomalies by NASA´s Gravity Recovery and Interior Laboratory (GRAIL) have confirmed the shallow presence of dense magma intrusions below floor-fractured craters on the Moon (Wieczorek et al., 2013).

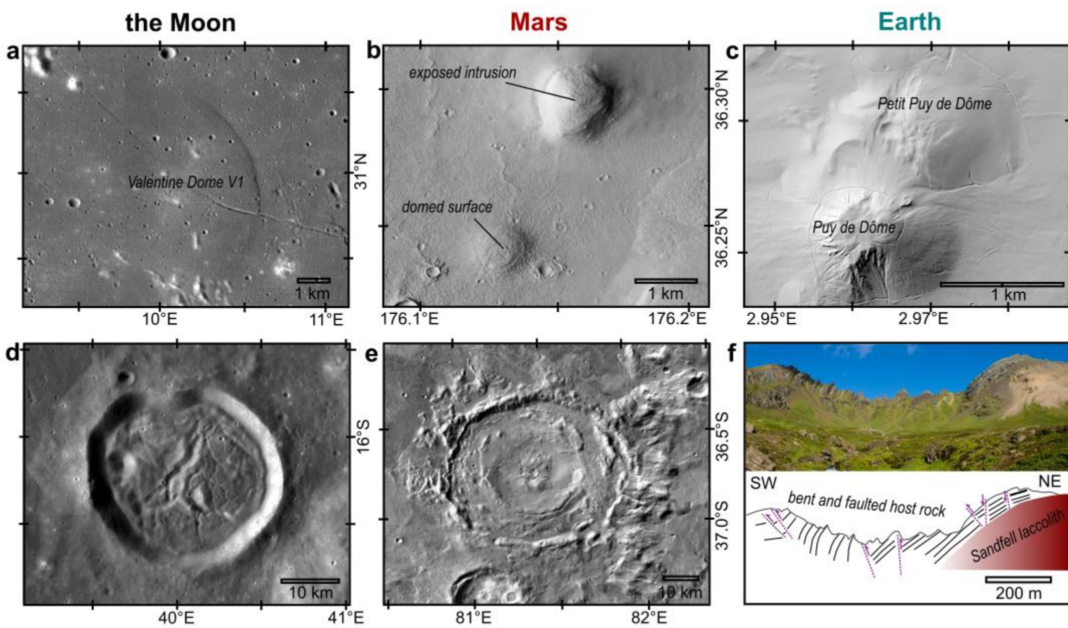

Fig. 1 *Magma-induced dome-shaped uplift features on three planetary bodies of different mass:* ***a.*** *Valentine 1 dome in Mare Serenitatis on the Moon (Lunar Reconaissance Orbiter (LRO), NASA);* ***b.*** *domed surface feature and exposed intrusion East of Phlegra Montes on Mars (Context Camera (CTX), NASA);* ***c.*** *hillshade relief image of the intrusive dome Petit Puy de Dôme and extrusive lava dome Puy de Dôme, Chaine-des-Pûys, France (LIDAR dataset www.craig.fr);* ***d.*** *lunar floor-fractured crater Bohnenberger (LRO, NASA);* ***e****. martian floor-fractured crater 28-000072 (Themis, NASA);* ***f.*** *image and interpretive sketch of the exposed Sandfell laccolith and bent and faulted host rocks in East-Iceland (after Mattsson et al., 2018).*

Existing analytical and numerical models assume a linearly-elastic response of the lunar and martian crust to magma-induced stresses (Bunger & Cruden, 2011; Grosfils et al., 2015; Michaut, 2011; Michaut & Pinel, 2018; Pollard & Johnson, 1973; Thorey & Michaut, 2016; Wöhler & Lena, 2009). Linearly-elastic behavior implies that rocks deform instantaneously and proportionally to stress, and may reverse to its initial state once the stress source is removed. Once the critical stress is exceeded, tensile fractures open and the rock ruptures (Jaeger et al., 2007; Segall, 2010). The geological observations at terrestrial laccoliths, however, such as at Sandfell in Iceland (Fig. 1f), show the importance of fracturing and faulting, besides elastic bending, of the overlying rocks (Mattsson et al., 2018; Wilson et al., 2016). The dome-shaped, uplifted surfaces Click or tap here to enter text.are often heavily dissected by faults and fractures, such as at the Petit Puy de Dôme in the Chaîne des Puys volcanic field in France (Fig. 1c) (Petronis et al., 2019).

The role of non-elastic deformation during intrusion inflation has been documented in scaled laboratory experiments where surface deformation can be directly related to the intrusion of analog magma as thick sills, laccoliths and cryptodomes in granular, cohesive materials (Currier & Marsh, 2015; Montanari et al., 2017; Poppe et al., 2019; Schmiedel et al., 2017). Furthermore, magnetic crystal fabrics in now-solidified and exposed viscous magma in Iceland and Argentina show that laccoliths can grow through repetitive magma pulses of high ascent rates and week- to month-long pauses during which the magma partially cools and solidifies (Burchardt et al., 2019; Mattsson et al., 2018). Such crustal accommodation through displacement, straining and fracturing often allows for more than doubling of the intruded magma volume without eruption.

The geological, geophysical and experimental observations outlined above have motivated the implementation of more complex stress responses though, such as elastoplasticity (Daniels et al., 2012; Scheibert et al., 2017). High concentrations of strain, and dynamic fracturing, can be simulated in the Discrete Element Method (DEM) (Cundall & Strack, 1979). The DEM discretizes a medium into an assemblage of spherical disks or spheres of which the position at each timestep is calculated according to Newton's laws of motion(Cundall & Strack, 1979). Unlike Finite Element Models (FEM), the DEM allows for the concentrations of large strains, discontinuous deformation and the dynamic opening and propagation of tensile fractures and shear bands. The particle assembly can thus be modelled to respond mechanically similarly to natural rock (Cundall & Strack, 1979; Potyondy & Cundall, 2004; Schöpfer et al., 2009). DEM has been used to simulate, amongst others, lava dome effusion and stability, hydraulic fracture propagation, or caldera collapse (Harnett et al., 2020; Harnett & Heap, 2021; Holohan et al., 2015; Huang et al., 2022; Morgan & McGovern, 2005; Woodell et al., 2023). Using two-dimensional (2D) DEM simulations, Morand et al. (2024) recently showed how mechanical properties control the surface displacement magnitudes and fracture network development during laccolith growth on Earth.

Accounting for nonelastic deformation and dynamic fracturing during laccolith inflation may be especially impactful for planets and moons smaller than Earth, where lower global mass results in lower gravitational acceleration compared to that on Earth. Compilations of rock deformation experiments have shown that reduced surface gravity leads to increased porosity and, consequentially, reduced brittle and tensile strength for similar depths (Heap et al., 2017). Models that assume linear elasticity during laccolith inflation (Bunger & Cruden, 2011; Michaut & Pinel, 2018; Walwer et al., 2021; Wöhler & Lena, 2009), have thus not clarified what the effect is of specific gravity on the development of crustal fracturing and surface displacements during the inflation of a laccolith.

We present simulations of the inflation of a laccolith at one kilometer depth under gravitational acceleration for Earth, Mars and the Moon with a 2D DEM model. We vary the strength of the host particle assemblage to represent a range of planetary crustal strengths. In this way, our 2D DEM implementation allows, for the first time, to discuss the effect of gravity as a function of planetary body mass and crustal strength on the magma-induced crustal deformation, dynamic fracturing, and surface displacement patterns.Click or tap here to enter text.

2 Method

2.1 Model set-up

We implemented the inflation of a laccolith-shaped magma intrusion in the commercial two-dimensional (2D) DEM Particle Flow Code (PFC2D 7.0) from Itasca Consulting Group, Ltd. (https://www.itascacg.com/software/PFC). Spherical particles with radii normally distributed around a mean of 6.65 ± 1.65 m were generated in a rectangular model domain of 20 km wide and 1 km high, constrained by lateral and bottom walls and with a free upper surface (Fig. 2). We assigned particles either to a class of rock, or magma. Contacts between two rock particles and between rock particles and the model walls were governed by the soft-bond model (Jiang et al., 2015; Ma & Huang, 2018a). This contact model represents a nonelastic solid medium defined by a bond effective modulus E*, bond tensile strength, bond cohesion (kept 10 times the bond tensile strength in our model such that contacts only break in tension), and two softening parameters (Ma & Huang, 2018b). All other numerical parameters were kept constant in our model (see Supplementary Table S1). The two softening parameters were kept constant to approach a 10:1 ratio of unconfined compressive strength to tensile strength in accordance with laboratory experiments on intact rock samples (Heap et al., 2021). We further followed the method of initialization of a stable particle assemblage as described by Harnett & Heap (2021) and Morand et al. (2024).

The absolute values of the rock particle bond strength parameters differ from the bulk strength of the simulated rock. Here, we simulated a range of realistic strengths of planetary crust, not one particular rock strength. To define the particle bond strength parameters needed to obtain the desired bulk properties, we performed numerical uniaxial compressive strength (UCS) and tensile strength (TS) tests (Harnett & Heap, 2021; Ma & Huang, 2018a; Morand et al., 2024). The obtained UCS, TS and Young´s modulus (E) values correspond to values measured on intact samples of natural rocks (Table 1), and are used to label figures 3 – 6. The DEM bond strength parameter values affect two properties of the rock strength. The toughness relates to the resistance of the rock to cracking (mainly controlled by the bond cohesion and bond tensile strength at a 10:1 ratio); tougher rocks can accommodate more strain before breaking. The stiffness relates to the resistance of the rock to elastic bending (mainly controlled by the bond effective modulus and ratio of normal to shear stiffness); stiffer rocks require more force to obtain a given amount of displacement and strain. We simulated six combinations of three rock toughnesses (TS of 0.8 ± 0.1 MPa, 1.9 ± 0.2 MPa, or 3.7 ± 0.1 MPa) for two rock stiffnesses (Young´s modulus of 2.5 ± 0.1 GPa or ~8.4 GPa) (Table 1). These ranges represent ranges of realistic elastic moduli, tensile strength and unconfined compressive strength obtained for intact rock samples scaled up to that of the weaker crust of a rocky planetary body, that is fractured and layered (Heap et al., 2017, 2020, 2021).

Magma particles were assigned within a body with a horizontal base with a width of 1,000 m, and a half-ellipse shaped convex roof with a top height of 50 m (Fig. 2). This laccolith was positioned at the bottom center of the model, and with its central top 1,000 m deep below the upper free surface. Contacts between two magma particles, between a rock and magma particle, and between magma particles and the lower model interface were defined by the linear parallel bond model, with zero friction, zero cohesion, zero tensile strength but a high effective modulus E*. This approach approximates the behavior of incompressible magma (Morand et al., 2024).

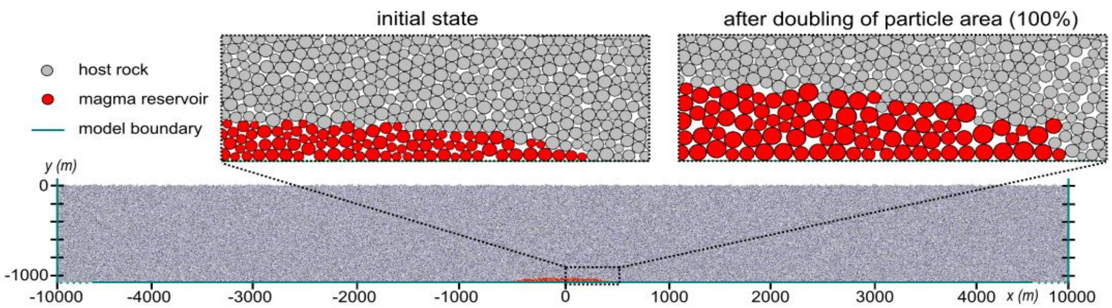

Fig. 2 *Model set-up implemented in the two-dimensional Discrete Element Method (2D DEM) in PFC2D (Itasca Ltd.) with an assemblage of host rock particles (grey) and a particle-based, half-ellipsoid-shaped magma body (red) with its top at 1 km depth. The subset images display the initial state and final state of the magma body after doubling of the magma particle area, i.e. after 100% of laccolith inflation.*

2.2 Model exploitation

We aimed to investigate the effect of the inflation of a laccolith on the shallow crust in function of gravity. We thus ran 2D DEM simulations that are subjected to the gravitational acceleration constant g of Earth (9.81 $m.s^{-2}$), Mars (3.71 $m.s^{-2}$), or the Moon (1.62 $m.s^{-2}$). We incrementally increased the area of the circular magma particles in the laccolith in steps of 1% until an area inflation of 100% was obtained (Fig. 2). Assuming an axial intrusion symmetry, this represents the doubling of laccolith volume from ~0.1 km^3 to ~0.2 km^3. This approach of particle area change is similar to that used to simulate the deflation of a magma body (Holohan et al., 2011, 2015), but differs from that of Harnett et al. (2020) and Morand et al. (2024), wherein new particles were added from below to inflate the lava dome or laccolith.

The inflating laccolith exerted stress on the surrounding rock particles, which were displaced. As a consequence, rock-rock contacts were strained. Particles resisted relative rotation which simulated a rigid interface between them. Once strained rock particle bonds failed, the soft-bond model was replaced by a rolling-resistance model that was only governed by a friction coefficient of 0.5 but with zero bond cohesion or bond tensile strength. This is analogue to strain-induced opening of tensile cracks and displacement of the detached rock masses along the crack plane in natural rock.

2.3 Model visualization and analysis

Particle position, velocity, displacement, bond stresses and bond cracking are tracked throughout the model. By convention, upward and rightward displacements are positive; downward and leftward displacements are negative. Cracks are formed by bond breakage (i.e. when the tensile bond strength is exceeded). In post-processing, the displacement gradient tensor is used to determine the finite shear strain from the Cauchy-Green deformation tensor (Schöpfer et al., 2006), further described by Harnett et al. (2018) and Morand et al. (2024). To emphasize the relative shear strain distribution within a simulation, we normalize all finite shear strain values to the simulation´s maximum. We further apply a cutoff criterion to all plots wherein all normalized finite shear strain values higher than 0.05% are set to 0.05%, because more than 90 % of finite shear strain values lies below that value. We express the number of cracked bonds as a percentage of the initial amount of rock particle bonds. To determine the maximum lateral extent of the vertically displaced surface in Table 1, all surface particles are included that are vertically displaced by more than 0.5% of the maximum vertical displacement value detected in the final time step of the simulation.

3 Results

3.1 Influence of gravity on magma-induced deformation

We systematically analyzed the patterns of magma-induced displacement (Fig. 3), and of vertical and horizontal displacement at the surface (Fig. 4). We provide figures displaying the final model outcome, the total displacements, stress, strain, and crack patterns for each simulation in the Online Supplementary materials.

We first discuss the displacement results irrespective of the value of gravitational acceleration. All displaced overburden rock areas are the narrowest near the magma-rock contact and the widest at the surface, and are laterally delimited by one or a series of en-echelon fractures. The inward dip of those fractures is the steepest for weak rocks (Fig. 3a-c, 3j-l) and the most gentle for the toughest rocks (Fig. 3g-i, 3p-r). Consequently, the displaced area is the widest in the toughest rock (Fig. 3g-i, 3p-r). In those toughest rocks, the displacement magnitude decreases continuously laterally outwards, we observe the longest and widest fractures, and also the widest displacement zones at the surface (Fig. 4i-l). Weaker rocks display discontinuities along which the displacement magnitude abruptly decreases laterally outwards from the model centre (Fig. 3a-i). Under these conditions, the vertical and horizontal displacement varies stepwise (Fig. 4a-h), in contrast with the continuous decrease laterally outwards in the toughest rocks (Fig. 4i-l). The locations of those stepwise variations in surface displacement magnitude correspond to open fractures at the model surfaces seen in Figure 3.

We then discuss the displacement results in function of specific gravity. The inward dip of the fractures that laterally delimit the displaced rock is the steepest for the highest gravity (Earth) (e.g., Fig. 3i) and the most gentle for the lowest gravity (the Moon) (e.g., Fig. 3g). Consequently, the displaced area is the widest at the lowest gravity where the bounding fractures do not reach the surface any longer but propagate horizontally away from the inflating laccolith (Fig. 3g, 3p). At that lowest gravity, the maximum of the displacement magnitude is the highest at 50 m, the extent of displacement at the surface is the widest and the slope of the vertical surface displacement curve is declining the steepest away from the center (Fig. 4, black curves). Under these lower-gravity conditions, the stepwise variations in horizontal displacement are also the largest across open surface fractures (Fig. 4b, 4d, 4f, 4h). In weaker rocks, the maxima of vertical displacement are 10-15 m higher at lower gravity on the Moon compared to those at Earth´s higher gravity (Fig. 4a, 4e); the maxima of horizontal displacement are 4-6 m lower (Fig. 4b, 4f). There is less difference in absolute values at the domes´ crests for stronger rocks across gravities (Fig. 4g-l). Displacement magnitudes and surface displacements for the intermediate gravity specific to Mars are overall intermediary between those on the Moon and on Earth. Only for Earth´s higher gravity we observe a central block near the surface bound by normal faults with less positive vertical displacement than the dome flanks and near-zero horizontal displacement (Fig. 4a-f).

Table 1. *Summary of bond strength and bulk strength values and key results for the 18 performed 2D DEM simulations.*

Model setup	***Bond parameters***			***Mechanical properties***				***Model results***		
Gravity g (m.s^{-2})	**E* (GPa)**	**Coh (MPa)**	**Ten (MPa)**	**E (GPa)**	**UCS (MPa)**	**TS (MPa)**	**UCS/ TS**	**Final U_y^{max} (m)**	**Lateral extent of U_y (km)**	**Fracture pattern End-member**
-1.62	3.0	10.0	1.0	2.5 ± 0.1	6.6 ± 0.9	0.8 ± 0.1	8.3 ± 2.0	40.0	3.699	Type 1
-3.71	3.0	10.0	1.0	2.5 ± 0.1	6.6 ± 0.9	0.8 ± 0.1	8.3 ± 2.0	36.9	3.903	Type 1
-9.81	3.0	10.0	1.0	2.5 ± 0.1	6.6 ± 0.9	0.8 ± 0.1	8.3 ± 2.0	26.1	4.330	Type 1
-1.62	3.0	25.0	2.5	2.5 ± 0.1	19.8 ± 3.5	1.9 ± 0.2	10.4 ± 2.6	46.3	4.735	Type 1
-3.71	3.0	25.0	2.5	2.5 ± 0.1	19.8 ± 3.5	1.9 ± 0.2	10.4 ± 2.6	37.2	4.328	Type 1
-9.81	3.0	25.0	2.5	2.5 ± 0.1	19.8 ± 3.5	1.9 ± 0.2	10.4 ± 2.6	28.0	4.211	Type 1
-1.62	3.0	50.0	5.0	2.5 ± 0.1	43.6 ± 6.0	3.7 ± 0.4	11.8 ± 2.6	40.4	5.723	Type 2
-3.71	3.0	50.0	5.0	2.5 ± 0.1	43.6 ± 6.0	3.7 ± 0.4	11.8 ± 2.6	37.6	4.670	Mixed
-9.81	3.0	50.0	5.0	2.5 ± 0.1	43.6 ± 6.0	3.7 ± 0.4	11.8 ± 2.6	37.2	4.191	Mixed
-1.62	10.0	10.0	1.0	8.4 ± 0.2	6.6 ± 0.9	0.8 ± 0.1	8.3 ± 2.0	43.5	3.537	Type 1
-3.71	10.0	10.0	1.0	8.4 ± 0.2	6.6 ± 0.9	0.8 ± 0.1	8.3 ± 2.0	40.0	3.942	Type 1
-9.81	10.0	10.0	1.0	8.4 ± 0.2	6.6 ± 0.9	0.8 ± 0.1	8.3 ± 2.0	35.6	3.821	Type 1
-1.62	10.0	25.0	2.5	8.4 ± 0.2	19.8 ± 3.5	1.9 ± 0.2	10.4 ± 2.6	42.5	4.923	Type 1
-3.71	10.0	25.0	2.5	8.4 ± 0.2	19.8 ± 3.5	1.9 ± 0.2	10.4 ± 2.6	38.0	4.242	Type 1
-9.81	10.0	25.0	2.5	8.4 ± 0.2	19.8 ± 3.5	1.9 ± 0.2	10.4 ± 2.6	39.5	3.791	Type 1
-1.62	10.0	50.0	5.0	8.4 ± 0.2	43.6 ± 6.0	3.7 ± 0.4	11.8 ± 2.6	39.5	7.813	Type 2
-3.71	10.0	50.0	5.0	8.4 ± 0.2	43.6 ± 6.0	3.7 ± 0.4	11.8 ± 2.6	42.3	4.702	Type 1
-9.81	10.0	50.0	5.0	8.4 ± 0.2	43.6 ± 6.0	3.7 ± 0.4	11.8 ± 2.6	39.1	4.045	Type 1

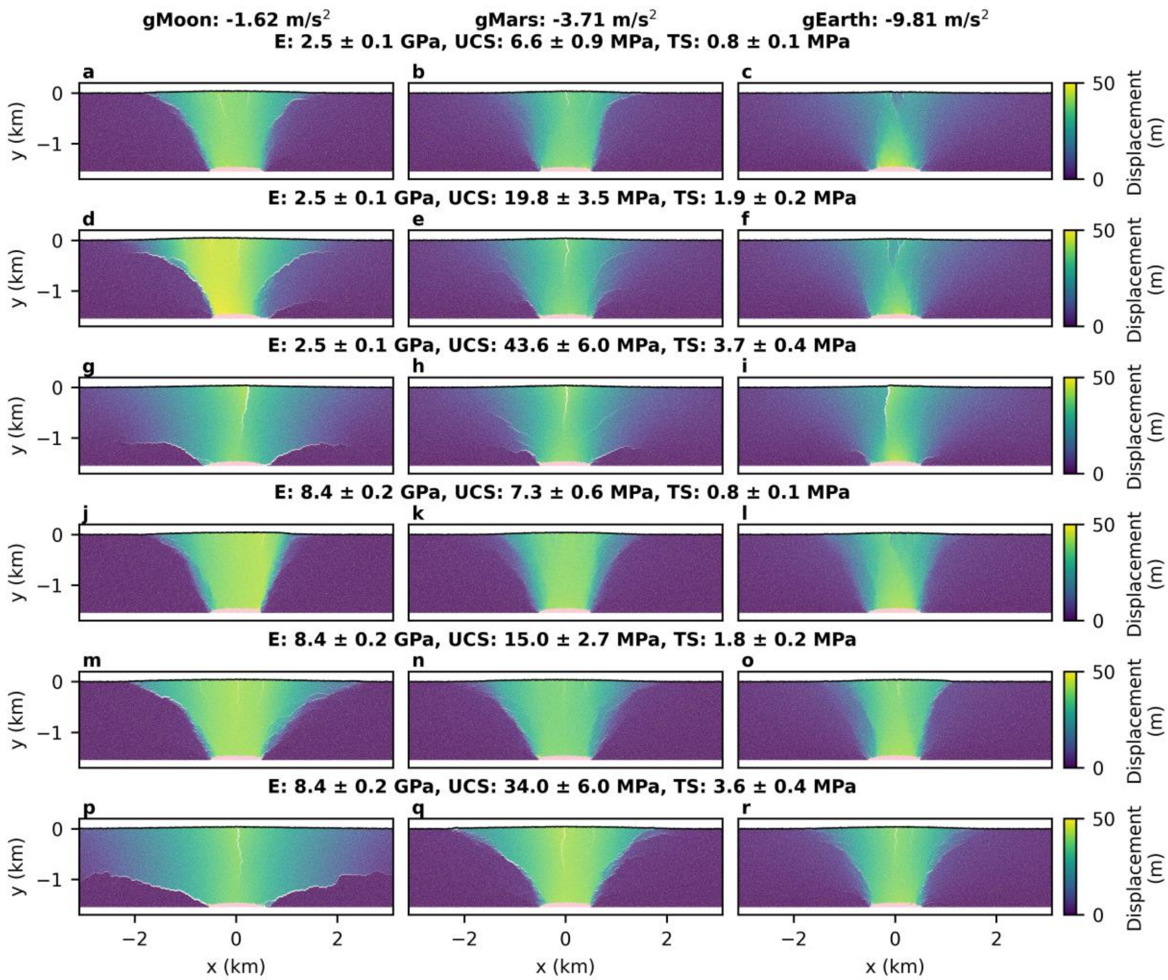

***Fig. 3** Displacement magnitude after doubling of the magma body area in the 2D DEM simulations subjected to gravity specific to the Moon, Mars, or Earth for a range of host rock Young´s moduli (E), unconfined compressive strengths (UCS) and tensile strengths (TS). Specific gravity increases from left to right, rock strength increases from top to bottom. Rock stiffness is the lowest in the three top rows and the highest in the three bottom rows.*

3.2 Influence of gravity on magma-induced strain and cracking

We first discuss the calculated normalized finite shear strain and cracking irrespective of the value of gravitational acceleration. For the same stiffness, less tough rocks accumulate the least shear strain and are the most cracked (Fig. 5a-c, 5j-l), whereas tougher rocks accumulate the most shear strain and crack the least (Fig. 5g-i, 5p-r). The fracture zones in which cracks concentrate are the widest in less tough rocks and the narrowest in tougher rocks. The zones of highest shear strain are the narrowest in less tough rocks and the narrowest in tougher rocks. As observed above, the fracture zones that delimit the deformed rock zone above the inflating laccolith are the steepest in less tough rocks (Fig. 5a-c, 5j-l), and the most gentle to subhorizontal in the tougher rocks (Fig. 5g-i, 5p-r). Quantitatively, less cracks open in less stiff rocks (up to 3.5% of initial bonds broken) (Fig. 6a-c), compared to more cracks in stiffer rocks (up to 6.5% of initial bonds broken) (Fig. 6d-f). For the same stiffness, more cracks open in less tough rocks (4.5% – 6.5%) (Fig. 6a, 6d), compared to less cracks in tougher rocks (0.5% – 2.5%) (Fig. 6c, 6f).

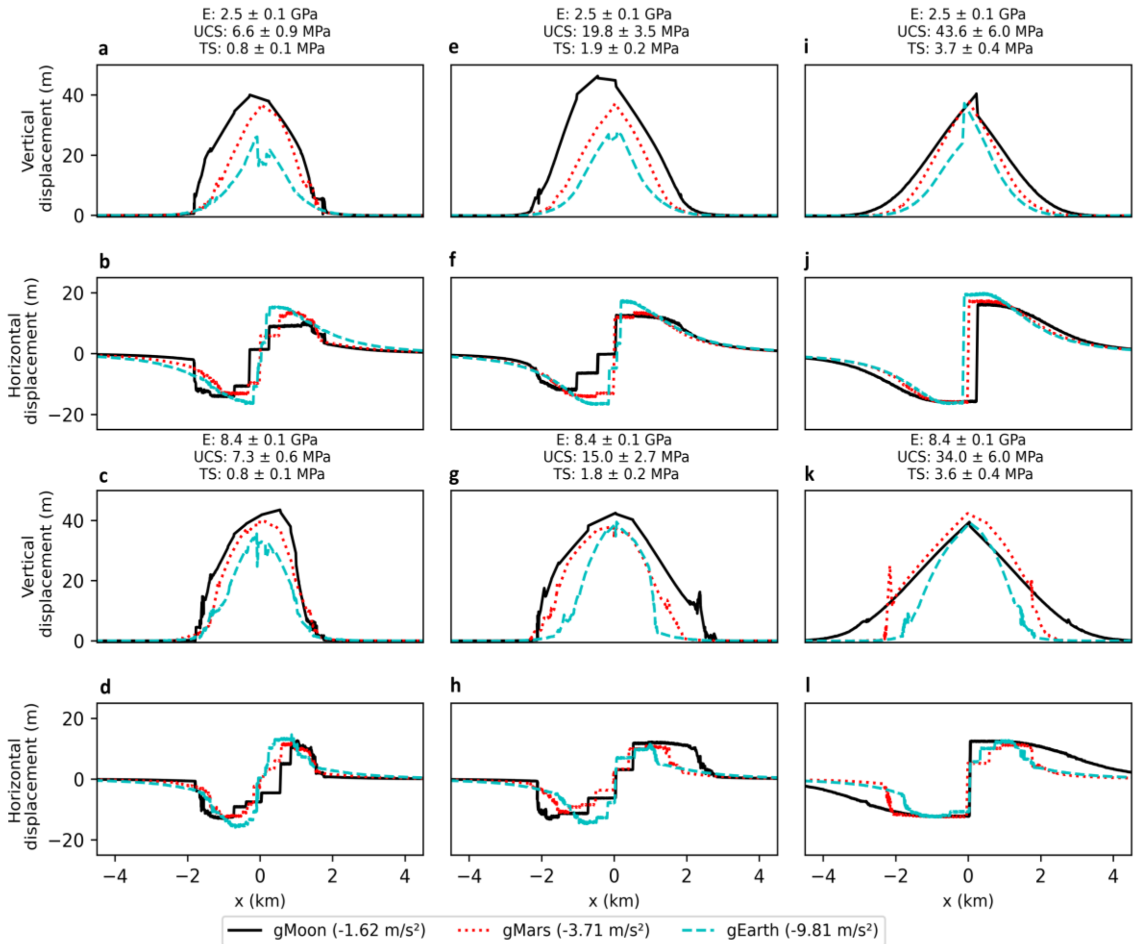

Fig. 4 *Horizontal and vertical surface displacement after doubling of the magma body area in 2D DEM simulations subjected to gravity specific to the Moon (black), Mars (red), or Earth (blue) for a range of host rock Young´s moduli (E), unconfined compressive strengths (UCS) and tensile strengths (TS). Toughness increases from the left column to the right column, stiffness increases from the top two rows to the bottom two rows. Gravity specific to each planetary body is indicated by line color and dashing.*

We then discuss the calculated normalized finite shear strain and cracking in function of specific gravity. For the same stiffness, rocks accumulate the least shear strain and are the least cracked at lower gravity specific to the Moon (Fig. 5a, 5d, 5g, 5j, 5m, 5p), whereas rocks accumulate the most shear strain and crack the most at higher gravity specific to Earth (Fig. 5c, 5f, 5i, 5l, 5o, 5r). The zones that delimit the deformed rock area in which shear strain and cracks concentrate are the narrowest at lower gravity and the widest at higher gravity. As observed above, the fracture zones that delimit the deformed rock zone above the inflating laccolith are the most gentle to subhorizontal at the lowest gravity and the steepest at the highest gravity. Time series of finite shear strain and crack pattern development (see Supplementary videos) show that the tensile fracture that opens at the crest of the uplifted surface propagates the deepest with the largest width at the lowest gravity (compare Fig. 5g-i and Fig. 5p-r). At the higher gravity and stiffer rocks, narrow bands of high finite shear strain remain uncracked (Fig. 5r).

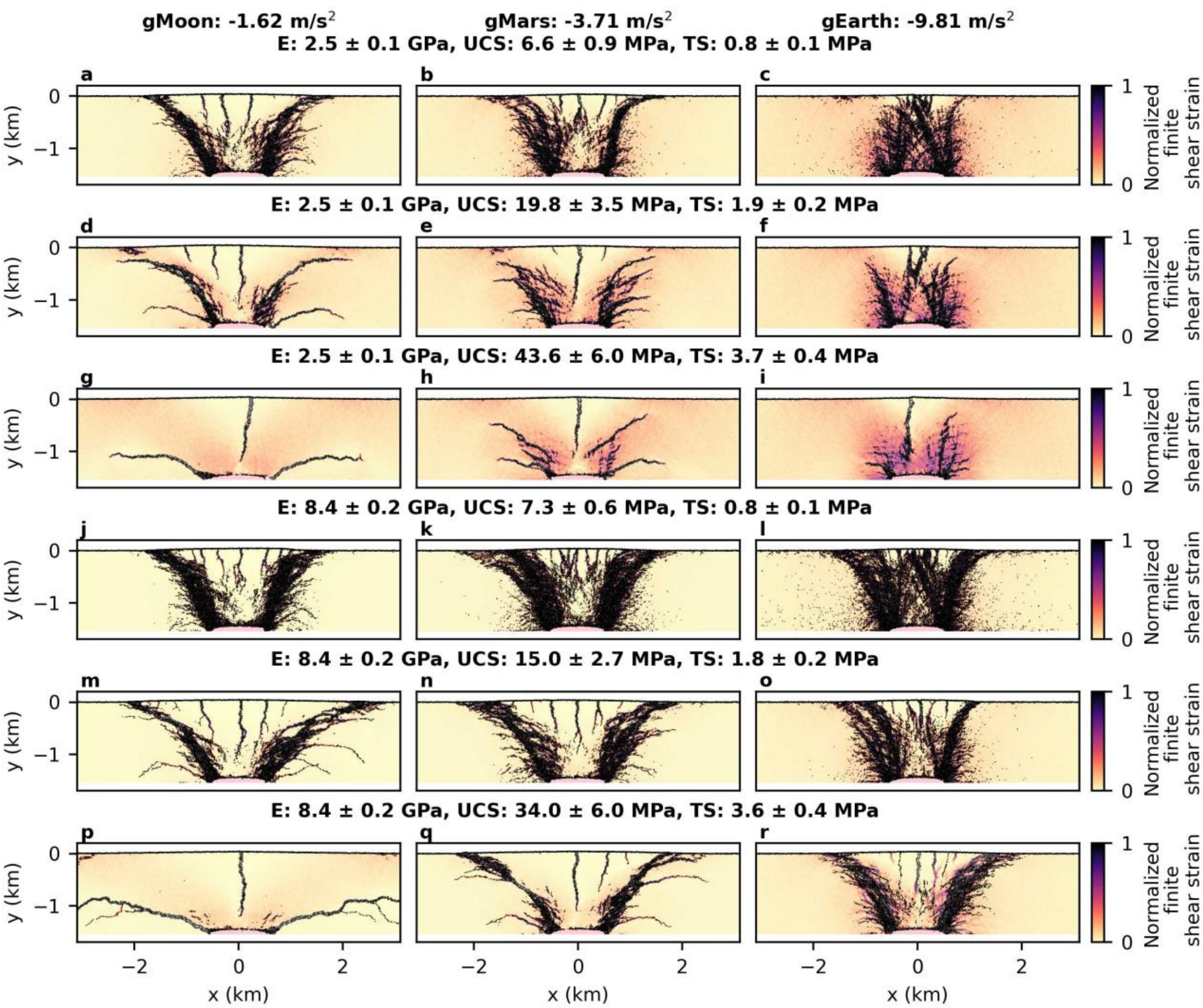

Fig. 5 *Normalized finite shear strain (see color bars) and cracked particle bonds (black lines) after doubling of the magma body area in the 2D DEM simulations subjected to gravity specific to the Moon, Mars, or Earth for a range of host rock Young´s moduli (E), unconfined compressive strengths (UCS) and tensile strengths (TS).*

Quantitatively, less cracks open at the lower gravity (Fig. 6, black curves), compared to more cracks opening at higher gravity (Fig. 6, blue curves). Crack amounts increases faster – the rock cracks more rapidly when stressed – at lower gravity than at high gravity in weak rocks (Fig. 6a), but in contract crack amounts increase faster at higher gravity in tougher and stiffer rocks (Fig. 6b-c, 6e-f). The difference between the amount of cracks in function of gravity is the highest with 2% for the strongest rocks (Fig. 6f). Notably, there is no significant difference in amount of cracks in function of specific gravity in the weakest rocks (Fig. 6a), but the spatial fracture and shear strain pattern is markedly different (Fig. 5a-c). Overall, Martian rocks respond in an intermediate manner to the inflation of the laccolith, compared to those on the Moon and Earth.

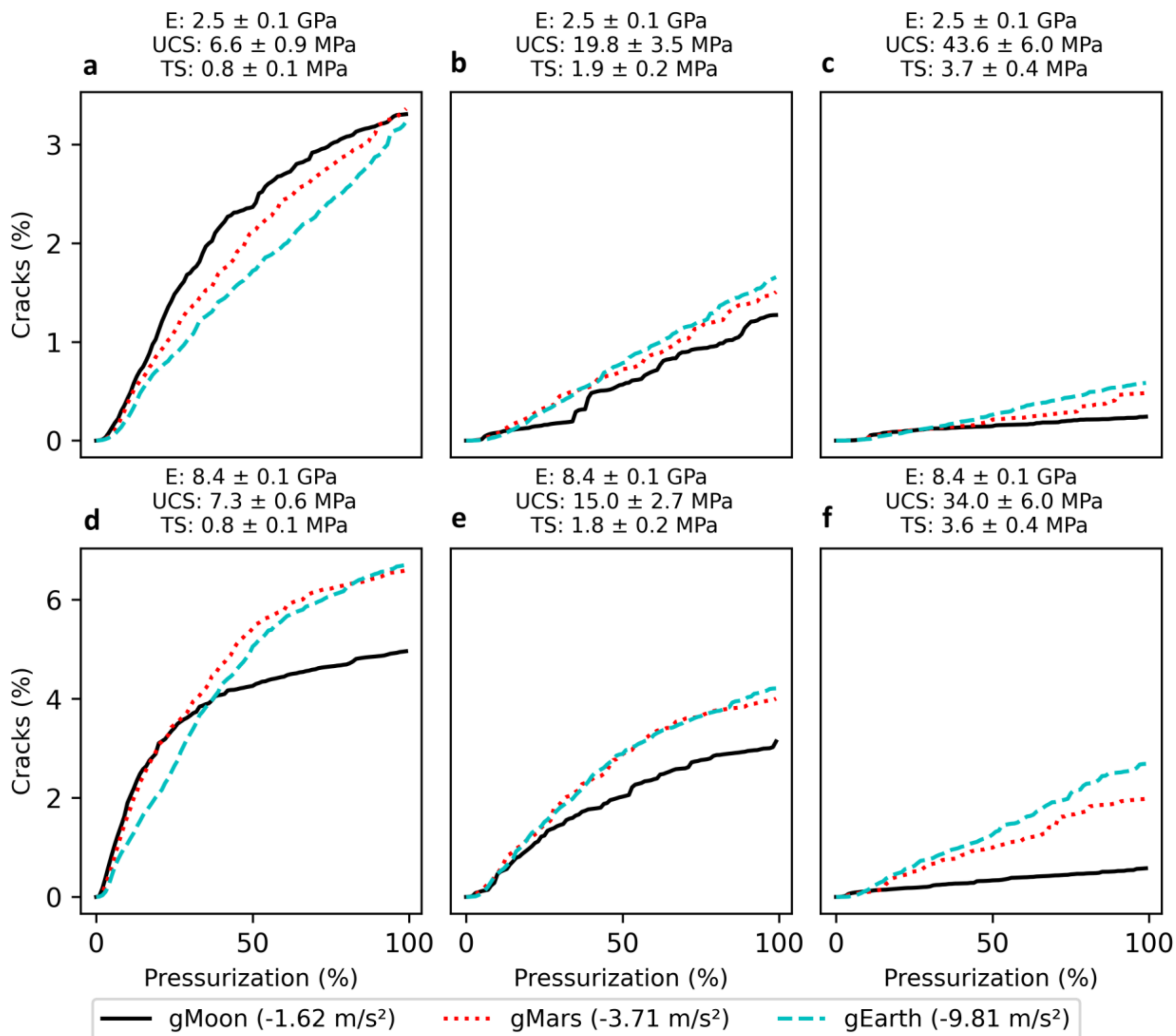

Fig. 6 *Development of cracks (failed particle bonds) during the inflation of the magma body area in 2D DEM simulations subjected to gravity specific to the Moon, Mars, or Earth for a range of host rock Young´s moduli (E), unconfined compressive strengths (UCS) and tensile strengths (TS).*

4 Discussion

The results from our 18 2D DEM simulations show that the spatial distribution and intensity of cracking of host rocks induced by the inflation of a laccolith of similar volume at similar depth lies along a spectrum between two end-members. Morand et al. (2024) attributed this spectrum to differences in the host rock toughness and stiffness. We show that the end-member spectrum is also controlled by the difference in gravitational acceleration between planetary bodies of different mass, here the Moon, Mars, and Earth. The first end-member develops a highly fractured host rock, with multiple tensile fractures that open from the surface downward into the host rock and two well-developed, inward-dipping shear fracture zones that develop from the laccolith edges and surface as thrust faults that bound the uplifted surface area (e.g., Fig. 3r, Fig. 5r). The second end-member develops a poorly fractured host rock, with one tensile fracture that opens from the surface downward at the crest of the uplifted surface area, and two inward-dipping to near-horizontal fractures that open from the intrusion edges outward (e.g.; Fig. 3p, Fig. 5p). When similarly tough crust is assumed (TS of ~3.7 MPa in our models), the deformation pattern approaches the first, highly fractured end-member rather for higher gravity on Earth and Mars, and the second, poorly fractured end-member for lower gravity on the Moon (Fig. 3p-r, Fig. 5p-r). For less tough crust (TS below 2.0 MPa in our models), we mainly see the most displacements and a highly fractured first end-member especially for lower gravity on the Moon.

Our model results show, however, that the linearly-elastic assumption is not compatible with syn-intrusive dynamic fracturing dynamics, wherein narrower bounding zones concentrate shear strain and close-spaced cracking at lower gravity on the Moon than on Earth (Fig. 5). The fracture and shear strain zones that develop from the edges of the inflating laccolith, grow upward and truncate the surface as reverse faults, except in the second end-member. These bounding fracture zones effectively laterally constrain the displaced and strained overburden rock, and once that lateral constraint has developed, the overburden can be displaced upward in coherent zones separated by one or more tensile fractures that propagate from the surface downward. The width of the displaced surface area thus becomes delimited by the fracturing dynamics in the host rock, which in turn is controlled by the gravity, and thus lithostatic loads at similar depth, specific to the planetary body the laccolith is inflating in. We observe less cracking when laccoliths inflate at lower gravity on the Moon, where the magma-induced stress is rather accommodated by upwards crustal displacement than by fracturing. As a result, we observe more surface displacement over a wider area on the Moon, compared to Earth, with Mars intermediate between the two.

Standard models that invert the surface displacements to obtain the diameter, but also the depth and opening of sills and laccoliths, simplify the crustal response to that of a homogeneous, linearly-elastic half-space (Battaglia et al., 2013; Mogi, 1958; Okada, 1985). Those analytical solutions do not involve a gravitational constant, whereas our model results demonstrate a significant effect of gravity on the surface displacements. More recent analytical and finite element models do include a gravitational constant (Fernández et al., 1997; Galland & Scheibert, 2013; Got et al., 2019; Michaut, 2011). Models at a similar Young´s modulus of 10 GPa than ours find more displacement over a wider area above laccoliths on the Moon compared to Earth

(Michaut, 2011). The slope of the domed surface is overall more gentle in those models for lower gravity, however, than in our models. All these models ignore fracturing dynamics, or only include a damage criterion (Got et al., 2019). It has been inferred that, because lunar intrusive surface doming features are wider than terrestrial ones, magmatic laccoliths and sills in the shallow lunar crust may be wider on the Moon than they are on Earth (Wohler & Lena 2009). Our 2D DEM results nevertheless show that concentrations of high strains and dynamic fracturing can narrow the width of the displaced surface area, especially for less tough rocks. This finding raise the expectation that those models may overestimate the width and depth of laccoliths on the Moon and Mars as compared to Earth. Direct comparisons between existing models and our DEM model, using the same strength properties, are now required to directly determine the difference between model outcomes that include, or ignore, dynamic fracturing.

We noted in the results that only our models for Earth´s gravity show a central area at the crest of the domed surface that is bound by opposing normal faults and that has been uplifted less than the surrounding area, i.e., a graben (Figs. 3, 4). The subsurface crack distribution is much more distributed in these conditions compared to those at lower gravities (Fig. 5). Geological observations at exposed igneous plumbing systems, seismic reflection data, and recent volcanic events on Earth, have shown that such graben systems can form as elongated topographic depressions above vertical, magma-filled fractures (dykes) (Magee & Jackson, 2021; Mastin & Pollard, 1988; Sigmundsson et al., 2014; Smittarello et al., 2022). Existing analytical models have used the geometry of such grabens observed on orbital imagery of the Moon or Mars to postulate that the lower gravity there would favor wider opening of higher dykes (Ernst et al., 2001; Head & Wilson, 1993; Klimczak, 2014). The height and opening of those tensile fractures in the crust of Mars or the Moon, versus those on Earth, is not well constrained though (Klimczak, 2015). Tensile fractures in our simulations open wider and propagate deeper from the surface downward on the Moon, and to lesser on Mars, than they can on Earth, for similar amounts of laccolith inflation (Fig. 3, Fig. 5). This progressive fracturing mechanism was not simulated previously, but the relative easiness of propagating open fractures deeper into the crust, in combination with impact-induced surface unloading (Michaut & Pinel, 2018; Wöhler & Lena, 2009), may have favored the ascent of dense mafic magma to the surface despite a negative buoyancy contrast with the porous shallow lunar crust.

Our new 2D DEM implementation will allow future simulations to investigate the interaction between extensional crustal stresses and impact-induced unloading, and laccolith-induced stresses. Simulations of broad ranges of laccolith thickness and width are also necessary to investigate if our conclusions hold for the widths of tens of kilometers of intrusive domes and floor-fractured craters found on the Moon and Mars. Our simulations furthermore do not account for the effects of magma viscosity and cooling on flow dynamics and geometric development of laccoliths found previously (Burchardt et al., 2019; Mattsson et al., 2018; Michaut, 2011; Thorey & Michaut, 2016). To investigate such effects on the dynamics of host rock fracturing and displacements will require a different approach for simulating magma flow and laccolith growth that goes beyond this work and that of (Morand et al., 2024). Constraints on the porosity, and thus strength, of the lunar and martian crust, remain a source of uncertainty, however, because they are either theoretical, or based on orbital observations, modeling of limited planetary seismic data, or laboratory experiments on terrestrial rocks (Heap et al., 2017; Q. Huang & Wieczorek, 2012; Knapmeyer-Endrun et al., 2021; Wieczorek et al., 2022). It remains necessary, therefore, as we have done here, to include a wide range of rock toughnesses and stiffnesses, in numerical simulations of tectonic and magma-induced deformation of the crust of Mars, the Moon and other rocky planetary bodies.

Finally, our 2D DEM models are the first to directly simulate dynamic fracturing and the concentration of high strains induced by an inflating laccolith under gravitational forces on planetary bodies of different mass. The results only do so along a vertical 2D profile. Three-dimensional DEM simulations of caldera and sinkhole collapse have shown how asymmetrical and anisotropic stresses and fracture patterns can develop (Hardy, 2021; Wang et al., 2022). This limits the nterpretation of fracture patterns and displacement patterns observed from orbit on the Moon and Mars. Future 3D DEM modeling will be required to better understand the development of asymmetric surface doming (Lena et al., 2013), hierarchical crack patterns at floor-fractured craters (Montigny et al., 2022), and the accuracy of using elastic rheology theory to infer intrusion depth from observed surface fracture patterns (Walwer et al., 2021).

5 Conclusions

We ran unprecedented 2D DEM simulations of displacement, straining and fracturing of planetary crust of a range of stiffness and toughness, by inflating a laccolith at one kilometer depth. Our simulations show that the different gravitational acceleration on the Moon, Mars, and Earth influences the magma-induced displacement patterns, as well as the concentration of shear strain and cracking in the subsurface. A same amount of magma emplaced at the same depth in the lunar or martian crust must have induced higher surface displacement compared to what is expected on Earth. This influence of the gravitational acceleration impacts estimates of volumes of magma intruded into the shallowest few kilometers of crust on the Moon and Mars. The amount of laccolith-induced cracking is, however, more dominantly controlled by the stiffness and toughness of the planetary crust, as found previously for Earth (Morand et al., 2024). Our model results show that inferrences on magma intrusion properties in the often already fractured and heterogeneous crusts of planetary bodies smaller than Earth, based on existing models that assume simplified crustal rheologies, should be assessed with caution.

Acknowledgments

S.P., A.C., and A.M. received funding from the Norwegian Financial Mechanism 2014–2021 (project “DeMo-Planet” 2020/37/K/ST10/02447) through the Polish National Science Centre (NCN Poland). S.P. acknowledges a postdoctoral ULAM scholarship for 2021-2023 from the Polish National Agency for Academic Exchange (NAWA) and an internal grant for 2024 from the Space Research Centre of the Polish Academy of Sciences (SRC PAS/CBK PAN). This work was initiated during the Erasmus+ exchange of A.C. in 2023, supported by internal funding from SRC PAS. Since 2024, A.M. received funding from the European Research Council (ERC) under the European Union's Horizon 2020 research and innovation programme (MAST; grant agreement No. 101003173). C.E.H. provided original scripts in PFC2D which we adapted to simulate laccolith inflation. Itasca Ltd. provided a discounted academic license of their commercial PFC2D software. Discussions with D. Mège, W. Kofman, M.J. Heap, M. Petronis, M. Awdankiewicz, C. Michaut helped improve our work.

Open Research

The authors declare no conflicts of interest relevant to this study. The simulations were produced under an academic license in the commercial software PFC2D (Itasca Ltd.) of which the code cannot be shared publicly. Python scripts used to plot the figures and process the simulation output, as well as the simulation output itself such as particles' positions, displacements, stresses, finite shear strain, radius and group of particles, and cracks' positions, orientations, length and aperture, will be made available in ASCII (.txt) format in a Zenodo data set (Poppe et al., in prep.).

References

Bamberg, M., Jaumann, R., Asche, H., Kneissl, T., & Michael, G. G. (2014). Floor-fractured craters on mars - Observations and origin. *Planetary and Space Science*, *98*, 146–162. https://doi.org/10.1016/j.pss.2013.09.017

Battaglia, M., Cervelli, P. F., & Murray, J. R. (2013). Modeling crustal deformation near active faults and volcanic centers-a catalog of deformation models. *US Geological Survey Techniques and Methods, Book 13*, 96. Retrieved from http://pubs.usgs.gov/tm/13/b1/

Brož, P., Hauber, E., Platz, T., & Balme, M. (2015). Evidence for Amazonian highly viscous lavas in the southern highlands on Mars. *Earth and Planetary Science Letters*, *415*, 200–212. https://doi.org/10.1016/j.epsl.2015.01.033

Bunger, A. P., & Cruden, A. R. (2011). Modeling the growth of laccoliths and large mafic sills: Role of magma body forces. *Journal of Geophysical Research: Solid Earth*, *116*(2), 1–18. https://doi.org/10.1029/2010JB007648

Burchardt, S., Mattsson, T., Palma, J. O., Galland, O., Almqvist, B., Mair, K., et al. (2019). Progressive Growth of the Cerro Bayo Cryptodome, Chachahuén Volcano, Argentina—Implications for Viscous Magma Emplacement. *Journal of Geophysical Research: Solid Earth*, *124*(8), 7934–7961. https://doi.org/10.1029/2019JB017543

Castro, J. M., Cordonnier, B., Schipper, C. I., Tuffen, H., Baumann, T. S., & Feisel, Y. (2016). Rapid laccolith intrusion driven by explosive volcanic eruption. *Nature Communications*, *7*, 13585. https://doi.org/10.1038/ncomms13585

Cundall, P. A., & Strack, O. D. L. (1979). A discrete numerical model for granular assemblies. *Géotechnique*, *29*(1), 47–65. https://doi.org/10.1680/geot.1979.29.1.47

Currier, R. M., & Marsh, B. D. (2015). Mapping real time growth of experimental laccoliths: The effect of solidification on the mechanics of magmatic intrusion. *Journal of Volcanology and Geothermal Research*, *302*, 211–224. https://doi.org/10.1016/j.jvolgeores.2015.07.009

Daniels, K. A., Kavanagh, J., Menand, T., Sparks, R. S. J., Daniels, K. A., Kavanagh, J., et al. (2012). The shapes of dikes : Evidence for the influence of cooling and inelastic deformation. *Geological Society of America Bulletin*, *124*(7/8), 1102–1112.

Ernst, R. E., Grosfils, E. B., & Mège, D. (2001). Giant dike swarms: Earth, Venus, and Mars. *Annual Reviews in Earth and Planetary Science*, *29*, 489–534. https://doi.org/10.1146/annurev.earth.29.1.489

Farrand, W. H., Lane, M. D., Edwards, B. R., & Aileen Yingst, R. (2011). Spectral evidence of volcanic cryptodomes on the northern plains of Mars. *Icarus*, *211*(1), 139–156. https://doi.org/10.1016/j.icarus.2010.09.006

Farrand, W. H., Rice, J. W., Chuang, F. C., & Rogers, A. D. (2021). Spectral and geological analyses of domes in western Arcadia Planitia, Mars: Evidence for intrusive alkali-rich volcanism and ice-associated surface features. *Icarus*, *357*. https://doi.org/10.1016/j.icarus.2020.114111

Fernández, J., Rundle, J. B., Granell, R. D. R., & Yu, T.-T. (1997). Programs to compute deformation due to a magma intrusion in elastic-gravitational layered Earth models. *Computers & Geosciences*, *23*(3), 231–249. https://doi.org/10.1016/S0098-3004(96)00066-0

Galland, O., & Scheibert, J. (2013). Analytical model of surface uplift above axisymmetric flat-lying magma intrusions: Implications for sill emplacement and geodesy. *Journal of Volcanology and Geothermal Research*, *253*, 114–130. https://doi.org/10.1016/j.jvolgeores.2012.12.006

Galland, O., Holohan, E. P., van Wyk de Vries, B., & Burchardt, S. (2018). Laboratory Modelling of Volcano Plumbing Systems: A Review. In C. Breitkreuz & S. Rocchi (Eds.), *Physical Geology of Shallow Magmatic Systems - Dykes, Sills and Laccoliths* (pp. 147–214). Springer Berlin Heidelberg.

Gilbert, G. K. (1877). *Geology of the Henry Mountains*. Washington, D.C.

Got, J. L., Amitrano, D., Stefanou, I., Brothelande, E., & Peltier, A. (2019). Damage and Strain Localization Around a Pressurized Shallow-Level Magma Reservoir. *Journal of Geophysical Research: Solid Earth*, *124*(2), 1443–1458. https://doi.org/10.1029/2018JB016407

Grosfils, E. B., Mcgovern, P. J., Gregg, P. M., Galgana, G. A., Hurwitz, D. M., Long, S. M., & Chestler, S. R. (2015). Elastic models of magma reservoir mechanics: A key tool for investigating planetary volcanism. *Geological Society Special Publication*, *401*, 239–267. https://doi.org/10.1144/SP401.2

Hall, J. L., & Solomon, S. C. (1981). Lunar Floor-Fractured Craters: Evidence for Viscous Relaxation of Crater Topography. *Journal of Geophysical Research*, *86*(B10), 9537–9552.

Hardy, S. (2021). Discrete element modelling of pit crater formation on mars. *Geosciences (Switzerland)*, *11*(7). https://doi.org/10.3390/geosciences11070268

Harnett, C. E., & Heap, M. J. (2021). Mechanical and topographic factors influencing lava dome growth and collapse. *Journal of Volcanology and Geothermal Research*, *420*, 107398. https://doi.org/10.1016/j.jvolgeores.2021.107398

Harnett, C. E., Benson, P. M., Rowley, P., & Fazio, M. (2018). Fracture and damage localization in volcanic edifice rocks from El Hierro, Stromboli and Tenerife. *Scientific Reports*, *8*(1). https://doi.org/10.1038/s41598-018-20442-w

Harnett, C. E., Heap, M. J., & Thomas, M. E. (2020). A toolbox for identifying the expression of dome-forming volcanism on exoplanets. *Planetary and Space Science*, *180*(September 2019), 104762. https://doi.org/10.1016/j.pss.2019.104762

Head, J. W., & Wilson, L. (1993). *Lunar graben formation due to near-surface deformation accompanying dike emplacement Introduction and background*. *Planet. Space Sci* (Vol. 41).

Head, J. W., & Wilson, L. (2017). Generation, ascent and eruption of magma on the Moon: New insights into source depths, magma supply, intrusions and effusive/explosive eruptions (Part 2: Predicted emplacement processes and observations). *Icarus*, *283*, 176–223. https://doi.org/10.1016/j.icarus.2016.05.031

Heap, M. J., Byrne, P. K., & Mikhail, S. (2017). Low surface gravitational acceleration of Mars results in a thick and weak lithosphere : Implications for topography , volcanism , and hydrology. *Icarus*, *281*, 103–114. https://doi.org/10.1016/j.icarus.2016.09.003

Heap, M. J., Villeneuve, M., Albino, F., Farquharson, J. I., Brothelande, E., Amelung, F., et al. (2020). Towards more realistic values of elastic moduli for volcano modelling. *Journal of Volcanology and Geothermal Research*, *390*, 106684. https://doi.org/10.1016/j.jvolgeores.2019.106684

Heap, M. J., Wadsworth, F. B., Heng, Z., Xu, T., Griffiths, L., Aguilar Velasco, A., et al. (2021). The tensile strength of volcanic rocks: Experiments and models. *Journal of Volcanology and Geothermal Research*, *418*. https://doi.org/10.1016/j.jvolgeores.2021.107348

Holohan, E. P., Schöpfer, M. P. J., & Walsh, J. J. (2011). Mechanical and geometric controls on the structural evolution of pit crater and caldera subsidence. *Journal of Geophysical Research: Solid Earth*, *116*(7), 1–23. https://doi.org/10.1029/2010JB008032

Holohan, E. P., Schöpfer, M. P. J., & Walsh, J. J. (2015). Stress evolution during caldera collapse. *Earth and Planetary Science Letters*, *421*, 139–151. https://doi.org/10.1016/j.epsl.2015.03.003

Huang, L., Dontsov, E., Fu, H., Lei, Y., Weng, D., & Zhang, F. (2022). Hydraulic fracture height growth in layered rocks: Perspective from DEM simulation of different propagation regimes. *International Journal of Solids and Structures*, *238*(September 2021), 111395. https://doi.org/10.1016/j.ijsolstr.2021.111395

Huang, Q., & Wieczorek, M. A. (2012). Density and porosity of the lunar crust from gravity and topography. *Journal of Geophysical Research: Planets*, *117*(5). https://doi.org/10.1029/2012JE004062

Ivanov, M. A., Head, J. W., & Bystrov, A. (2016). The lunar Gruithuisen silicic extrusive domes: Topographic configuration, morphology, ages, and internal structure. *Icarus*, *273*, 262–283. https://doi.org/10.1016/j.icarus.2015.12.015

Jaeger, J. C., Cook, N. G. W., & Zimmerman, R. W. (2007). *Fundamentals of Rock Mechanics*. *Cambridge University Press* (Vol. 1). https://doi.org/10.1017/CBO9781107415324.004

Jiang, M., Shen, Z., & Wang, J. (2015). A novel three-dimensional contact model for granulates incorporating rolling and twisting resistances. *Computers and Geotechnics*, *65*, 147–163. https://doi.org/10.1016/j.compgeo.2014.12.011

Jozwiak, L. M., Head, J. W., Zuber, M. T., Smith, D. E., & Neumann, G. A. (2012). Lunar floor-fractured craters: Classification, distribution, origin and implications for magmatism and shallow crustal structure. *Journal of Geophysical Research E: Planets*, *117*(11), 1–23. https://doi.org/10.1029/2012JE004134

Kavanagh, J. L., Burns, A. J., Hilmi Hazim, S., Wood, E. P., Martin, S. A., Hignett, S., & Dennis, D. J. C. (2018). Challenging dyke ascent models using novel laboratory experiments: Implications for reinterpreting evidence of magma ascent and volcanism. *Journal of Volcanology and Geothermal Research*, *354*, 87–101. https://doi.org/10.1016/j.jvolgeores.2018.01.002

Klimczak, C. (2014). Geomorphology of lunar grabens requires igneous dikes at depth. *Geology*, *42*(11), 963–966. https://doi.org/10.1130/G35984.1

Klimczak, C. (2015). Limits on the brittle strength of planetary lithospheres undergoing global contraction. *Journal of Geophysical Research: Planets*, *120*(12), 2135–2151. https://doi.org/10.1002/2015JE004851

Knapmeyer-Endrun, B., Panning, M., Bissig, F., Joshi, R., Khan, A., Kim, D., et al. (2021). Thickness and structure of the Martian crust from InSight seismic data. *Advancement of Science*, *373*(6553), 438–443. https://doi.org/10.1126/science.abf8966ï

Lena, R., Wöhler, C., Phillips, J., & Chiocchetta, M. T. (2013). *Lunar Domes*. Milano: Springer Milan. https://doi.org/10.1007/978-88-470-2637-7

Ma, Y., & Huang, H. (2018a). A displacement-softening contact model for discrete element modeling of quasi-brittle materials. *International Journal of Rock Mechanics and Mining Sciences*, *104*, 9–19. https://doi.org/10.1016/j.ijrmms.2018.02.007

Ma, Y., & Huang, H. (2018b). DEM analysis of failure mechanisms in the intact Brazilian test. *International Journal of Rock Mechanics and Mining Sciences*, *102*(November 2017), 109–119. https://doi.org/10.1016/j.ijrmms.2017.11.010

Magee, C., & Jackson, C. A.-L. (2021). Can we relate the surface expression of dike-induced normal faults to subsurface dike geometry? *Geology*, *49*(4), 366–371. https://doi.org/https://doi.org/10.1130/G48171.1

Magee, C., Stevenson, C. T. E., Ebmeier, S. K., Keir, D., Hammond, J. O. S., Gottsmann, J. H., et al. (2018). Magma Plumbing Systems: A Geophysical Perspective. *Journal of Petrology*, (June), 1–35. https://doi.org/10.1093/petrology/egy064

Mastin, L. G., & Pollard, D. D. (1988). Surface deformation and shallow dike intrusion processes at Inyo Craters, Long Valley, California. *Journal of Geophysical Research*, *93*(B11), 13221–13235. https://doi.org/10.1029/JB093iB11p13221

Mattsson, T., Burchardt, S., Almqvist, B. S. G., & Ronchin, E. (2018). Syn-emplacement fracturing in the sandfell laccolith, eastern iceland—implications for rhyolite intrusion growth and volcanic hazards. *Frontiers in Earth Science*, *6*(February). https://doi.org/10.3389/feart.2018.00005

McGovern, P. J., Grosfils, E. B., Galgana, G. A., Morgan, J. K., Rumpf, M. E., Smith, J. R., & Zimbelman, J. R. (2014). Lithospheric flexure and volcano basal boundary conditions; keys to the structural evolution of large volcanic edifices on the terrestrial planets. *Volcanism and Tectonism across the Inner Solar System*, 19 p. https://doi.org/doi:10.1144/SP401.7

Michaut, C. (2011). Dynamics of magmatic intrusions in the upper crust: Theory and applications to laccoliths on Earth and the Moon. *Journal of Geophysical Research*, *116*(B5). https://doi.org/10.1029/2010jb008108

Michaut, C., & Pinel, V. (2018). Magma Ascent and Eruption Triggered by Cratering on the Moon. *Geophysical Research Letters*, *45*(13), 6408–6416. https://doi.org/10.1029/2018GL078150

Michaut, C., Baratoux, D., & Thorey, C. (2013). Magmatic intrusions and deglaciation at mid-latitude in the northern plains of Mars. *Icarus*, *225*(1), 602–613. https://doi.org/10.1016/j.icarus.2013.04.015

Michaut, C., Pinel, V., & Maccaferri, F. (2020). Magma ascent at floor-fractured craters diagnoses the lithospheric stress state on the Moon. *Earth and Planetary Science Letters*, *530*. https://doi.org/10.1016/j.epsl.2019.115889

Mogi, K. (1958). Relations between the eruptions of various volcanoes and the deformations of the ground surfaces around them. *Bulletin of the Earthquake Research Institute*. https://doi.org/10.1016/j.epsl.2004.04.016

Montanari, D., Bonini, M., Corti, G., Agostini, A., & Del Ventisette, C. (2017). Forced folding above shallow magma intrusions: Insights on supercritical fluid flow from analogue modelling. *Journal of Volcanology and Geothermal Research*, *345*, 67–80. https://doi.org/10.1016/j.jvolgeores.2017.07.022

Montigny, A., Walwer, D., & Michaut, C. (2022). The origin of hierarchical cracks in floor-fractured craters on Mars and the Moon. *Earth and Planetary Science Letters*, *600*. https://doi.org/10.1016/j.epsl.2022.117887

Morand, A., Poppe, S., Harnett, C., Cornillon, A., Heap, M., & Mège, D. (2024). Fracturing and Dome-Shaped Surface Displacements Above Laccolith Intrusions: Insights From Discrete Element Method Modeling. *Journal of Geophysical Research: Solid Earth*, *129*(3). https://doi.org/10.1029/2023JB027423

Morgan, J. K., & McGovern, P. J. (2005). Discrete element simulations of gravitational volcanic deformation: 1. Deformation structures and geometries. *Journal of Geophysical Research: Solid Earth*, *110*(5), 1–22. https://doi.org/10.1029/2004JB003252

Morgan, S. (2018). Pascal's Principle, a Simple Model to Explain the Emplacement of Laccoliths and Some Mid-crustal Plutons. *Volcanic and Igneous Plumbing Systems*, 139–165. https://doi.org/10.1016/B978-0-12-809749-6.00006-6

Okada, Y. (1985). Surface deformation due to shear and tensile faults in a half space. *Bulletin of the Seismological Society of America*, *75*(4), 1135–1154.

Petronis, M. S., van Wyk de Vries, B., & Garza, D. (2019). The leaning Puy de Dôme (Auvergne, France) tilted by shallow intrusions. *Volcanica*, *2*(2), 161–189. https://doi.org/10.30909/vol.02.02.161186

Platz, T., Byrne, P. K., Massironi, M., & Hiesinger, H. (2015). Volcanism and tectonism across the inner solar system: An overview. *Geological Society Special Publication*, *401*, 1–56. https://doi.org/10.1144/SP401.22

Pollard, D. D. (1973). Derivation and evaluation of a mechanical model for sheet intrusions. *Tectonophysics*, *19*(3), 233–269. https://doi.org/10.1016/0040-1951(73)90021-8

Pollard, D. D., & Johnson, A. M. (1973). Mechanics of growth of some laccolithic intrusions in the Henry Mountains, Utah, II: bending and failure of overburden layers and sill formation. *Tectonophysics*, *18*(3–4), 311–354.

Poppe, S., Holohan, E. P., Galland, O., Buls, N., Van Gompel, G., Keelson, B., et al. (2019). An Inside Perspective on Magma Intrusion: Quantifying 3D Displacement and Strain in Laboratory Experiments by Dynamic X-Ray Computed Tomography. *Frontiers in Earth Science*, *7*, 62. https://doi.org/10.3389/feart.2019.00062

Potyondy, D. O., & Cundall, P. A. (2004). A bonded-particle model for rock. *International Journal of Rock Mechanics and Mining Sciences*, *41*(8 SPEC.ISS.), 1329–1364. https://doi.org/10.1016/j.ijrmms.2004.09.011

Rampey, M. L., Milam, K. A., McSween, H. Y., Moersch, J. E., & Christensen, P. R. (2007). Identity and emplacement of domical structures in the western Arcadia Planitia, Mars. *Journal of Geophysical Research: Planets*, *112*(6). https://doi.org/10.1029/2006JE002750

Scheibert, J., Galland, O., & Hafver, A. (2017). Inelastic deformation during sill and laccolith emplacement: Insights from an analytic elastoplastic model. *Journal of Geophysical Research: Solid Earth*, *122*(2), 923–945. https://doi.org/10.1002/2016JB013754

Schmiedel, T., Galland, O., & Breitkreuz, C. (2017). Dynamics of Sill and Laccolith Emplacement in the Brittle Crust: Role of Host Rock Strength and Deformation Mode. *Journal of Geophysical Research: Solid Earth*, *122*(11), 8860–8871. https://doi.org/10.1002/2017JB014468

Schöpfer, M. P. J., Childs, C., & Walsh, J. J. (2006). Localisation of normal faults in multilayer sequences. *Journal of Structural Geology*, *28*(5), 816–833. https://doi.org/10.1016/j.jsg.2006.02.003

Schöpfer, M. P. J., Abe, S., Childs, C., & Walsh, J. J. (2009). The impact of porosity and crack density on the elasticity, strength and friction of cohesive granular materials: Insights from DEM modelling. *International Journal of Rock Mechanics and Mining Sciences*, *46*(2), 250–261. https://doi.org/10.1016/j.ijrmms.2008.03.009

Schultz, P. H. (1976). Floor-fractured lunar craters. *The Moon*, *15*(3–4), 241–273. https://doi.org/10.1007/BF00562240

Segall, P. (2010). *Earthquake and volcano deformation*. Princeton, New Yersey: Princeton University Press. https://doi.org/10.5860/choice.48-0287

Sigmundsson, F., Hooper, A., Hreinsdóttir, S., Vogfjörd, K. S., Ófeigsson, B. G., Heimisson, E. R., et al. (2014). Segmented lateral dyke growth in a rifting event at Bárðarbunga volcanic system, Iceland. *Nature*, *517*(7533), 15. https://doi.org/10.1038/nature14111

Smittarello, D., Smets, B., Barrière, J., Michellier, C., Oth, A., Shreve, T., et al. (2022). Precursor-free eruption triggered by edifice rupture at Nyiragongo volcano. *Nature*, *609*(September). https://doi.org/10.1038/s41586-022-05047-8

Thomas, R. J., Rothery, D. A., Conway, S. J., & Anand, M. (2015). Explosive volcanism in complex impact craters on Mercury and the Moon: Influence of tectonic regime on depth of magmatic intrusion. *Earth and Planetary Science Letters*, *431*, 164–172. https://doi.org/10.1016/j.epsl.2015.09.029

Thorey, C., & Michaut, C. (2016). Elastic-plated gravity currents with a temperature-dependent viscosity, 88–117. https://doi.org/10.1017/jfm.2016.538

Vaucher, J., Baratoux, D., Mangold, N., Pinet, P., Kurita, K., & Grégoire, M. (2009). The volcanic history of central Elysium Planitia: Implications for martian magmatism. *Icarus*, *204*(2), 418–442. https://doi.org/10.1016/j.icarus.2009.06.032

Walwer, D., Michaut, C., Pinel, V., & Adda-Bedia, M. (2021). Magma ascent and emplacement below floor fractured craters on the Moon from floor uplift and fracture length. *Physics of the Earth and Planetary Interiors*, *312*. https://doi.org/10.1016/j.pepi.2021.106658

Wang, T., Zhang, F., Furtney, J., & Damjanac, B. (2022). A review of methods, applications and limitations for incorporating fluid flow in the discrete element method. *Journal of Rock Mechanics and Geotechnical Engineering*, *14*(3), 1005–1024. https://doi.org/10.1016/j.jrmge.2021.10.015

Wieczorek, M. A., Neumann, G. A., Nimmo, F., Kiefer, W. S., Taylor, G. J., Melosh, H. J., et al. (2013). The crust of the Moon as seen by GRAIL. *Science*, *339*(6120), 671–675. https://doi.org/10.1126/science.1231530

Wieczorek, M. A., Broquet, A., Mclennan, S. M., Rivoldini, A., Golombek, M., Antonangeli, D., et al. (2022). InSight Constraints on the Global Character of the Martian Crust Journal of Geophysical Research : Planets, 1–35. https://doi.org/10.1029/2022JE007298

Wilhelms, D. E. (1987). The geologic history of the Moon. *U.S. Geological Survey Professional Paper*, *1348*, 1–293.

Wilson, P. I. R., McCaffrey, K. J. W., Wilson, R. W., Jarvis, I., & Holdsworth, R. E. (2016). Deformation structures associated with the Trachyte Mesa intrusion, Henry Mountains, Utah: Implications for sill and laccolith emplacement mechanisms. *Journal of Structural Geology*, *87*, 30–46. https://doi.org/10.1016/j.jsg.2016.04.001

Wöhler, C., & Lena, R. (2009). Lunar intrusive domes: Morphometric analysis and laccolith modelling. *Icarus*, *204*(2), 381–398. https://doi.org/10.1016/j.icarus.2009.07.031

Woodell, D. R., Schöpfer, M. P. J., & Holohan, E. P. (2023). Numerical models of restless caldera volcanoes. *Earth and Planetary Science Letters*, *621*. https://doi.org/10.1016/j.epsl.2023.118376

Supplementary Table S1. Varied computational parameters and corresponding rock properties in the 2D DEM model.

Model geometry	
Model width	20,000 m
Depth of laccolith top	1,000 m
Laccolith width	1,000 m
Laccolith height	50 m
Particle radii	6.65 ± 1.65 m
Number of particles	~120 x 10^3
PFC2D7 contact model	
Rock-rock	Soft-bond
Rock-wall	Soft-Bond
Magma-magma	Linear parallel bond
Magma-wall	Linear
Magma-rock	Linear parallel bond
Along broken bonds (cracks)	Rolling resistance linear
Bond parameters that control stiffness	
Effective modulus (E*)	2.5 x 10^9 (Pa) $^{\alpha}$
Ratio between normal and shear stiffness	2.5
Bond parameters that control toughness	
Bond tensile strength (ten)	0.0 (Pa) $^{\alpha}$
Bond cohesion (coh)	10 x bond tensile strength (Pa)
Other contact parameters	
Friction angle	Rock-rock/rock-wall: 30.0 (°) Rock-magma: 26.6 (°) Other bonds: 0.0 (°)
Friction coefficient between unbonded particles	Magma-magma/magma-wall: 0.0 Other bonds: 0.5
Softening factor (γ)	Rock-rock/rock-wall: 13
Softening tensile strength factor (ζ)	Rock-rock/rock-wall: 0.4
Radius multiplier	1.0
Gap between bonded particles	6.65 x 10^{-3} (m)

$^{\alpha}$ *for rock-rock bonds and rock-wall bonds, see Table 1 in the main text.*